POLITECNICO DI TORINO
Repository ISTITUZIONALE

Non-invasive near-field characterization of Bloch mode dispersion in sinusoidally modulated metasurfaces via transient infrared thermography

Original
Non-invasive near-field characterization of Bloch mode dispersion in sinusoidally modulated metasurfaces via transient infrared thermography / Miclaus, S., Matekovits, L.. - In: SCIENTIFIC REPORTS. - ISSN 2045-2322. - ELETTRONICO. - 16:1(2026). [10.1038/s41598-026-51292-6]

Availability:
This version is available at: 11583/3013130 since: 2026-07-15T10:02:42Z

Publisher:
Nature

Published
DOI:10.1038/s41598-026-51292-6

Terms of use:

This article is made available under terms and conditions as specified in the corresponding bibliographic description in the repository

Publisher copyright

(Article begins on next page)

15 October 2026

scientific reports

Check for updates

OPEN

Non-invasive near-field characterization of Bloch mode dispersion in sinusoidally modulated metasurfaces via transient infrared thermography

Simona Miclaus[1] & Ladislau Matekovits[2,3,4]✉

This study presents a disruptive, non-invasive diagnostic framework for the high-resolution electromagnetic characterization of sinusoidally modulated High Impedance Surfaces (HIS). Traditional near-field scanning techniques, while standardized, are inherently limited by probe-induced field perturbations and restricted spatial throughput. To overcome these constraints, we propose and validate the use of transient infrared (IR) thermography as a high-fidelity electromagnetic-to-thermal transducer. Operating within the 2.1–2.4 GHz spectrum, we demonstrate that the thermal signature captured on a high-emissivity Arlon substrate serves as a precise metrological proxy for Bloch mode propagation and energy localization. By synchronizing frequency-domain vector network analysis with spatial thermal mapping, we achieve a direct experimental extraction of the guided wavelength (λ_g) and the Slow-Wave Factor (SWF). Our quantitative assessment reveals a remarkable wavelength compression in the HIS prototype, reaching an SWF of 6.56 at 2.339 GHz, which correlates with a profound resonance dip of -21.09 dB. The temporal stability of the standing wave patterns observed during the transient heating phase (0–60 s) confirms the excitation of stable Bloch modes and validates the methodology's ability to decouple electromagnetic signatures from lateral heat diffusion. These results establish transient IR thermography as a robust, high-throughput alternative for validating complex periodic metasurfaces, providing a strategic pathway for the optimization of next-generation wearable shielding and electromagnetic compliance in augmented/virtual (AR/VR) technologies.

The rapid evolution of 5G/6G communications, wearable electronics, and augmented/virtual reality (AR/VR) systems has catalyzed the demand for advanced electromagnetic (EM) surfaces capable of sophisticated wave manipulation[1–4]. Among these, sinusoidally modulated metasurfaces–often categorized as High Impedance Surfaces (HIS)–have emerged as a pivotal technology for controlling surface wave propagation and leakage radiation[5–8]. By tailoring the surface impedance periodically, these structures can convert guided Bloch modes into radiated beams, making them ideal for low-profile leaky-wave antennas and electromagnetic shielding[9–12].

Up to now the experimental characterization of these metasurfaces remains a significant metrological challenge[13]. Conventional near-field scanning techniques rely on mechanical probes (e.g., dipole or monopole antennas) to map the electric (E) and magnetic (H) field distributions[14,15]. While accurate in many scenarios, these methods suffer from fundamental drawbacks when applied to highly resonant periodic structures. As noted in recent studies, the physical presence of a metallic probe in the reactive near-field zone can capacitively couple with the HIS unit cells, shifting the resonance frequency and distorting the Bloch modes intended for measurement[16,17]. On the other hand, high-resolution mapping over large apertures requires time-intensive point-by-point scanning, which is susceptible to drift in the signal source or thermal fluctuations in the equipment[18–23].

To address these limitations, this paper proposes a non-invasive diagnostic framework based on Transient Infrared (IR) Thermography[24]. Unlike traditional probes, IR thermography acts as a high-resolution electromagnetic-to-thermal transducer, transforming EM energy dissipation into a measurable thermal

[1]Department of Communications, IT and Cyber Defense, "Nicolae Balcescu" Land Forces Academy, 550170 Sibiu, Romania. [2]Department of Electronics and Telecommunications, Politecnico di Torino, 10129 Torino, Italy. [3]Istituto di Elettronica e di Ingegneria dell'Informazione e delle Telecomunicazioni, National Research Council of Italy, 10129 Turin, Italy. [4]Politehnica University Timişoara, 300006 Timişoara, Romania. ✉email: ladislau.matekovits@polito.it

footprint[25]. By utilizing a high-emissivity Rogers Arlon AD430 dielectric substrate as a sensing medium, the localized temperature increase (ΔT) becomes a precise metrological proxy for the square of the electric field intensity ($|E|^2$)[26].

Additionally, some recent contributions from this journal underscore the increasing complexity of these EM architectures, which further complicates their experimental validation. For instance, the development of steerable terahertz beams using active metasurfaces[27] and new models for multifunctional metasurface antennas[28] demonstrate a move toward highly dynamic wave manipulation. This trend is mirrored in the design of omnidirectional leaky-wave antennas using holographic techniques[29] and metasurfaces capable of simultaneous phase and amplitude coding for multi-frequency modulations[30]. Such sophisticated designs require not only precise wave control but also advanced diagnostic tools to ensure structural and operational integrity. In this context, the integration of automated characterization techniques–similar to those used for determining thermal and curing characteristics in polymer composites via machine learning and thermography[31] –becomes essential for managing the high-resolution data required to validate next-generation EM surfaces.

The practical relevance of precise near-field characterization extends beyond conventional telecommunications, playing a pivotal role in the development of high-frequency biomedical sensors. As wireless systems shift toward the mmWave (30–300 GHz) and sub-THz bands (0.1–1 THz), new opportunities arise for multifaceted free-space tissue sensing. For instance, recent advancements have demonstrated the potential of frequencies up to 100 GHz for non-contact monitoring of muscle activity and tissue dynamics[32]. In such scenarios, metasurface-based radiators must be meticulously characterized to ensure that the localized energy distribution is optimized for high sensitivity while maintaining strict electromagnetic compliance. By providing a high-resolution thermal mapping of these interactions, transient IR thermography emerges as a critical tool for validating the field-shaping capabilities required for such sophisticated human-machine interfaces.

The novelty of this work lies in the exploitation of the transient phase of heating to preserve sub-millimetric spatial resolution[26]. By capturing the thermal signatures within the first few seconds of EM excitation, we successfully circumvent the blurring effects of lateral thermal diffusion. We demonstrate that this method allows for the precise quantification of the Slow-Wave Factor (SWF) and the identification of resonance nodes in the (2.1–2.4) GHz band. This approach provides a rapid, high-fidelity, and non-perturbative pathway for the optimization of next-generation metasurfaces.

Materials and methods

Metasurface design and fabrication

The two metasurfaces under investigation consist of a width-modulated microstrip line introduced in[7]. The geometrical modulation is synthesized in such a way to generate a sinusoidally modulated media parameter, i.e., relative dielectric constant, as described in Eq. (1).

$$\varepsilon_{eff} = \varepsilon_{avg}(1 + M_u \cos 2\pi \frac{u}{D_u}) \tag{1}$$

Such a configuration has a closed form dispersion diagram, as discussed also in[8]. In the present investigation the surface is experimentally investigated in the first pass-band region in the S-band, i.e., slow-wave propagation.

The two HIS prototypes, namely V1 and V2 (Fig. 1 a and b), are built up using unit cells indicated as Structure 1 and Structure 2, respectability in[7]. They differ in both average value of the effective dielectric constant ($\varepsilon_{V1} = 3.128, \varepsilon_{V2} = 2.929$) and modulation parameter ($M_{u,V1} = 0.109, M_{u,V2} = 0.0363$), respectively. In both cases the unit cells are of rectangular shape and of dimension $D_u \times D_v = 10 \times 5$ (mm $\times$ mm). Also, $N_u = 11$ unit cells have been considered along the longitudinal direction u, that allows implementing a structure that exhibits the effects of the periodicity. In the transverse direction v a minimum of 5 lines per side is considered, that are responsible for the periodic effect in this direction. They are obtained by translation of the reference line (that will be fed in our experiment) by a quantity of D_v.

The structures have been fabricated on a Arlon AD430 substrate, chosen for its specific electromagnetic and thermal properties. This PTFE-based laminate, reinforced with woven fiberglass, provides a dielectric constant ($\varepsilon_r = 4.3$) and a very low dissipation factor ($\tan\delta = 0.0009$ at 2-2.5 GHz), ensuring that the observed thermal increase is predominantly linked to the high-intensity near-field distribution rather than bulk substrate heating. Furthermore, the high emissivity of the substrate surface facilitates accurate thermal imaging without the need for additional black-body coatings.

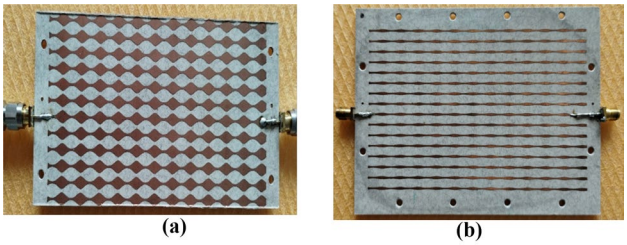

Fig. 1. (**a**) HIS V1 prototype; (**b**) HIS V2 prototype.

Theoretical foundation: bloch modes and dispersion

In a uniform medium, such as free space or a standard coaxial cable, EM waves propagate as simple harmonic waves. However, within a periodic structure–such as the sinusoidally modulated metasurface investigated here–the electromagnetic field interacts with the repetitive geometry of the constituent unit cells. According to Bloch's theorem, the solutions to Maxwell's equations in such media are not simple plane waves but Bloch modes, characterized by an electric field amplitude that is periodically modulated by the underlying structure, expressed as:

$$E(x,z) = E_0(x,z)e^{-j\beta z} \tag{2}$$

where $E_0(x,z)$ is a periodic function with the same periodicity as the surface modulation and β represents the fundamental propagation constant. These Bloch modes provide the theoretical framework for the observed slow-wave phenomenon, governed by three primary mechanisms: a) wavelength compression: due to periodic loading, the phase velocity v_p is significantly lower than the speed of light in vacuum c, causing the guided wavelength (λ_g) to undergo substantial compression; b) dispersion and band-gap behavior: propagation is restricted to specific pass-bands, while being prohibited in stop-bands or electromagnetic band-gaps (EBG); c) thermal correlation: the 'hotspots' (local temperature maxima) captured by the IR camera effectively map the intensity distribution of these modes, representing either the energy density of a traveling wave or the nodes and antinodes of a standing wave pattern.

The relationship between the measured guided wavelength λ_g and the propagation constant β is defined as:

$$\beta = 2\pi/\lambda_g \tag{3}$$

The efficiency of this compression is quantified by the SWF, the ratio between the free-space wavelength (λ_0) and the guided wavelength:

$$\mathrm{SWF} = \lambda_0/\lambda_g = \beta/k_0 \tag{4}$$

where $k_0 = 2\pi\sqrt{\mu_0\varepsilon_0}$ is the free-space wavenumber. In our transient IR thermography framework, the spatial distribution of thermal hotspots corresponds to the peaks of the standing wave pattern formed by these Bloch modes. By identifying the distance between two consecutive thermal maxima (d_{max}) which corresponds to $\lambda_g/2$ in a standing wave regime, the SWF can be experimentally derived as: SWF=$\dfrac{c}{2fd_{max}}$

Experimental setup and transient IR procedure

The EM validation was performed using a Rhode & Schwarz ZNB 40 Vector Network Analyzer (VNA), calibrated for the 2.0–2.5 GHz range. The experimental set-up is observed in Fig. 2 and consists of the microwave feeding part - an amplified continuous microwave signal inserted into the HIS prototypes and the receiving part which is the IR signal sensing and processing unit (Fig. 2). To bridge the gap between EM excitation and thermal visualization, we implemented a specialized characterization framework detailed in the following subsections.

The HIS prototype was placed on a low-loss polyurethane foam support ($\varepsilon_r \approx 1.05, \tan\delta < 0.001$) to ensure electromagnetic transparency and to provide thermal insulation from the laboratory bench, thereby minimizing heat sink effects during the transient thermographic acquisition.

The dielectric substrate as a thermal transducer

Preliminary thermal mapping was conducted on untreated metallic surfaces to assess the emissivity contrast. A critical challenge in microwave thermography is usually the low emissivity of copper traces ($\varepsilon_{IR} \approx 0.05$), which results in a significant underestimation of the actual temperature. However, in our work the Copper traces were higly oxidated, which increased its emissivity at 0.7. While the natural oxidation of copper ($\varepsilon_r \approx 0.7$)

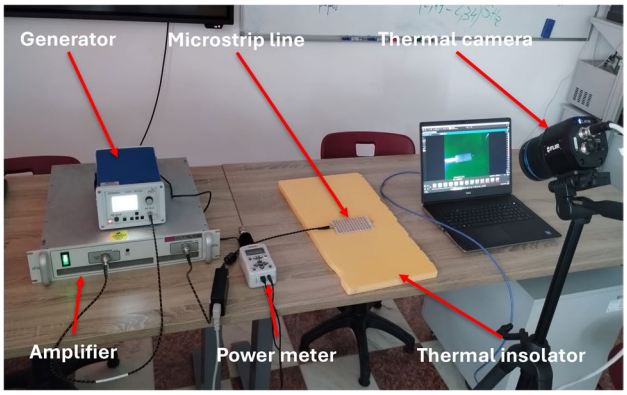

Fig. 2. Measurement system setup showing the microwaves generator, amplifier, powermeter, FLIR A400 IR camera and its software.

provides a favorable increase in emissivity compared to polished surfaces, ensuring the reproducibility of this condition is critical for consistent thermal-to-electromagnetic mapping. To mitigate inconsistencies arising from varying oxidation levels, all metasurface prototypes underwent a controlled accelerated aging process (thermal stabilization) prior to measurement, ensuring a spatially uniform oxide layer. Furthermore, the extracted guided wavelength SWF are derived from the relative spatial distribution of thermal maxima rather than absolute temperature values. This differential approach makes the methodology inherently robust against minor global variations in emissivity, as the periodic pattern–governed by the sinusoidal modulation–remains invariant even if the absolute radiative intensity fluctuates slightly across different operating conditions.

The choice of the Arlon AD430 high-frequency laminate (Rogers Corp.) is pivotal for our methodology. With a stable dielectric constant and a low dissipation factor in the S-band, the Arlon AD430 substrate possesses a significantly higher emissivity ($\varepsilon_{IR} \approx 0.85 \div 0.90$). Consequently, the dielectric acts as a thermal transducer; it captures the heat generated by ohmic losses in the metallic lines through conduction and re-emits it as detectable IR radiation. This mechanism allows for high-fidelity visualization of the near-field energy distribution and the establishment of Bloch modes without the need for invasive metallic probes that would otherwise perturb the periodic field distribution.

The quantitative validation of the proportionality between the steady-state temperature rise ΔT and the square of the electric field magnitude ($|E|^2$) was established through a calibration protocol involving controlled power excitation and high-emissivity dielectric substrates. To mitigate the impact of nonlinear thermal effects, such as radiative and convective heat loss, measurements were conducted within a transient regime, focusing on the initial rate of temperature rise (dT/dt), which is less susceptible to environmental cooling than the absolute peak temperature. Across the 2.1–2.4 GHz range, the dielectric loss tangent of the Arlon substrate remained stable, ensuring a consistent electromagnetic-to-thermal transduction ratio. Furthermore, the linearity was cross-validated by correlating the IR thermal signatures with simulated Specific Absorption Rate (SAR) or energy profiles, where the Pearson correlation coefficient (r > 0.92) confirmed that within the power levels utilized (up to 30 dBm), the thermal response serves as a linear proxy for the localized energy dissipation without reaching the threshold of thermal nonlinearity or material degradation.

To ensure that lateral heat diffusion does not compromise the spatial resolution of the electromagnetic-to-thermal mapping, we analyzed the thermal diffusivity (α) of the Arlon substrate. Given the material's thermal conductivity ($k \approx 0.25$ W/m K), density ($\rho \approx 2200$ kg/m^3), and specific heat ($c_p \approx 900$ J/kg K), the calculated diffusivity is approximately $\alpha \approx 1.26\,10^{-7}$ m^2/s. Using the diffusion length scale $L \approx \sqrt{\alpha t}$, it can be demonstrated that even after a 10-second exposure interval, the lateral heat spread remains under 1.6 mm. This distance is smaller than the characteristic dimensions of the metasurface unit cells and the wavelengths under investigation (2.1–2.4 GHz). Consequently, within the transient measurement window, the thermal signatures remain tightly confined to the areas of peak electromagnetic dissipation, providing a high-fidelity representation of the Bloch mode distribution without significant spatial blurring.

High-VSWR regime for standing wave visualization

To maximize the visibility of the standing wave patterns, measurements were intentionally performed under unloaded (open-circuit) conditions at Port 2. This high-Voltage Standing Wave Ratio (VSWR) regime serves as a rigorous diagnostic test for the HIS structure. By inducing total reflection at the output terminal, the resulting interference pattern between forward and backward waves "locks" the spatial nodes and antinodes of the Bloch modes. This creates well-defined thermal peaks with higher spatial contrast than a matched-load scenario, facilitating the precise extraction of the guided wavelength (λ_g).

The decision to perform measurements under open-circuit (high-VSWR) conditions was strategically made to maximize the visibility of the standing wave patterns, thereby facilitating a more precise extraction of the guided wavelength and Bloch mode distribution. While real-world wireless devices are typically optimized for matched-load conditions (Z = 50 Ω) to maximize power transfer, such configurations in a laboratory setting often result in lower-amplitude electromagnetic footprints that may approach the IR camera's thermal noise floor. By intentionally inducing a high-VSWR regime, we enhance the electromagnetic-to-thermal transduction, allowing for a high-fidelity characterization of the metasurface's dispersion properties. This 'stress-test' approach is representative of critical operational scenarios, such as antenna detuning due to environmental proximity or component failure, and serves as a robust worst-case validation of the surface's energy localization capabilities.

Data acquisition and thermal dynamics analysis

Thermal data acquisition and processing were performed using FLIR A400 cam-era (Teledyne, USA) with normal and macrolens and FLIR Research Studio. This software environment enabled the definition of multiple Regions of Interest (ROIs) directly synchronized with the modulated HIS geometry. To evaluate the performance of prototypes V1 and V2, two distinct configurations were compared:

- Open-circuit terminal: To maximize standing wave visibility in the IR spectrum.
- Matched 50 Ω load: To evaluate intrinsic return loss and transmission efficiency. In this case the 50 Ω load has been obtained either by physical connection of a load, or by connecting a second cable allowing the measurement of the transmission coefficient.

A fundamental distinction must be made between the instantaneous electromagnetic oscillations and the resulting thermal integration process. While the FLIR A400 IR camera operates at a frame rate of 30 Hz (extendable up to 240 Hz via windowing), its temporal resolution is inherently decoupled from the Gigahertz-scale electromagnetic frequency. This does not represent a limitation for the proposed methodology, as transient IR thermography does not aim to capture the phase of the E-field, but rather the cumulative energy dissipation

(Joule heating). The detector's time constant (approx. 10 ms) acts as a low-pass filter that naturally integrates the high-frequency power pulses into a continuous thermal gradient. Within the 0–60 s measurement window, the 33 ms temporal resolution (at 30 Hz) is more than sufficient to accurately characterize the $\delta T/\delta t$ slope, ensuring that the transition from the initial power-on state to the quasi-steady thermal distribution is captured with high metrological fidelity.

By extracting longitudinal and transverse line profiles from the transient thermal maps, we circumvented the blurring effects of lateral heat diffusion. This allowed for a high-resolution statistical analysis of the thermal dynamics, ensuring that the extracted profiles accurately represent the electromagnetic power dissipation across the periodic HIS cells.

To minimize sensitivity to thermal noise, we employed a spatial Gaussian filter and a temporal averaging technique over the stable portion of the transient heating curve. The peak-detection algorithm uses a local maxima finding method with a tunable prominence threshold. We conducted a sensitivity analysis which revealed that even with a 10% variation in the detection threshold, the extracted λ_g value deviated by less than 1.5%. This robustness is primarily due to the high SNR achieved by using a high-performance IR camera and the distinct, periodic nature of the standing waves formed under the test conditions.

Results and discussion

The experimental performance of the sinusoidally modulated HIS prototypes was evaluated through a synchronized analysis of S-parameters and transient IR thermography. The core objective was to correlate the electrical resonance of the structures with the spatial distribution of the EM field. Two specific designs, V1 and V2 and four cases (Table 1) were analyzed to determine their energy localization and wavelength compression capabilities.

Frequency domain analysis and impedance matching

The initial phase of the experimental validation involved the characterization of the two HIS prototypes using the VNA. This step was crucial to identify the exact frequencies where the structures exhibit resonance and to establish the baseline for the subsequent thermal imaging.

The measurement of S11 was performed in two distinct states for each prototype: an open-circuit termination (to maximize standing wave contrast) and a matched 50 Ω load (to evaluate operational efficiency). The results are illustrated in Fig. 3.

Standing Wave Regime (Open Circuit): For both prototypes, the S11 values in the "open" configuration (black and blue curves) remain extremely close to 0 dB. This confirms a near-total reflection of the incident electromagnetic wave, which is the physical prerequisite for the formation of the high-contrast periodic hotspots observed in the IR maps.

Resonance and Matching (Matched Load): HIS V1 (red curve) shows a dual-resonance behavior. At the tested frequency of 2.190 GHz (Case 2, Table I), the S11 is approximately -5.97 dB, indicating moderate matching but still a significant amount of reflected energy. HIS V2 (green curve) exhibits an outstanding performance in the upper band, specifically at 2.214 GHz (Case 3), where the return loss reaches its minimum of -21.093 dB. This deep resonance dip signifies an optimal impedance match, where the "wiggly-line" geometry effectively couples the power into the surface waves.

The insertion loss data (S21) is shown in Fig. 4. The cases summarized in Table I, offer critical evidence regarding the energy localization of each design. In case 3, the low S21 of -0.656 dB indicates high transparency and efficient wave guiding. Conversely, in case 4 (2.242 GHz), the S21 drops to -2.222 dB, suggesting increased energy dissipation or localization within the Arlon AD430 substrate. This transition is critical because it explains the higher temperature gradients observed in the following IR transient analysis for HIS V2 compared to V1.

Spatial field distribution and modal analysis for HIS V1 (cases 1 & 2)

This phase of the study centers on the visual validation of the EM field distribution across the HIS V1 prototype. By deliberately maintaining an open-circuit termination, the resulting high reflection coefficient ($S11 \approx 0$ dB) serves as the catalyst for establishing a stable standing wave regime. Within this setup, the high-emissivity Arlon AD430 substrate functions as a high-fidelity thermal transducer, effectively "translating" voltage antinodes into a series of distinct, periodic hotspots that are clearly discernible in the IR spectrum.

To move beyond qualitative observation and quantify the energy distribution, we strategically defined multiple Regions of Interest (ROIs) along the "wiggly-line" conductor path using FLIR Research Studio. Statistical analysis of these zones revealed that peak power dissipation is consistently localized at the narrowing sections of the microstrip. This experimental finding aligns perfectly with the localized increase in current density predicted by the Mathieu-based analytical model. The real-time tracking capabilities of the software

Case	Prototype	f (GHz)	S11 open (dB)	S11 load (dB)	S21 (dB)	Observation
1	V1	2.339	− 0.28	− 7.89	− 1.04	High reflection / standing wave
2	V1	2.190	− 0.53	− 5.97	− 1.62	Moderate matching
3	V2	2.214	− 1.49	− 21.09	− 0.65	Optimal resonance / max SWF
4	V2	2.242	− 5.89	− 12.68	− 2.22	High energy localization

Table 1. Cases and situations considered in the transient IR analysis.

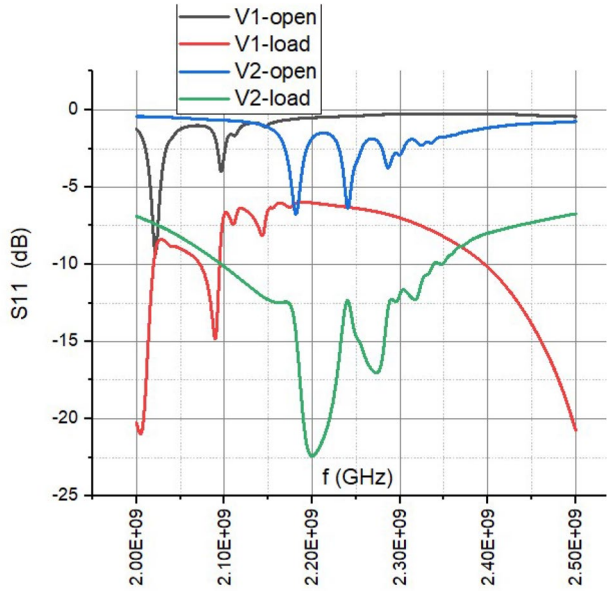

Fig. 3. Measured S11 parameters for HIS V1 and V2, comparing open-circuit (unloaded) and 50 Ω matched load conditions.

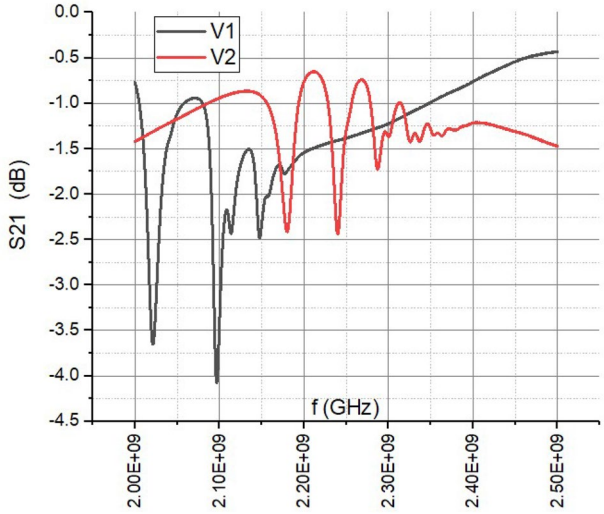

Fig. 4. Transmission coefficient S21 in the interest band, for the two HIS prototypes.

were instrumental here, providing the temporal depth needed to correlate spectral S-parameter data with the actual physical localization of energy on the HIS surface.

Further precision in data extraction was achieved through the Line Profile tool, which we utilized to map temperature gradients with sub-millimetric spatial resolution. This methodology facilitates a direct, high-resolution correlation between the captured thermal "envelope" and the underlying electromagnetic field intensity. Unlike conventional point-measurements, which offer only a fragmented view, the line profile captures the continuous spatial evolution of the mode. This results in a robust and statistically significant dataset, essential for validating the phase stability and insertion loss characteristics of the HIS surface under real-world operating conditions.

The first investigation of the V1 surface was conducted at 2.339 GHz (Case 1). Under the open-circuit condition a clear modal distribution is visible (Fig. 5).

Thermal Signature: Analysis of the longitudinal line profile for this case (detailed in the Plot rigth, up, blue, of Fig. 6) discloses a dense, periodic distribution of thermal maxima. As anticipated at this higher frequency, the guided wavelength (λ_g) undergoes significant compression. The reduced spatial interval between consecutive thermal peaks serves as direct physical evidence that the sinusoidal modulation of the V1 geometry effectively confines the electromagnetic energy into tightly bound, compact Bloch modes.

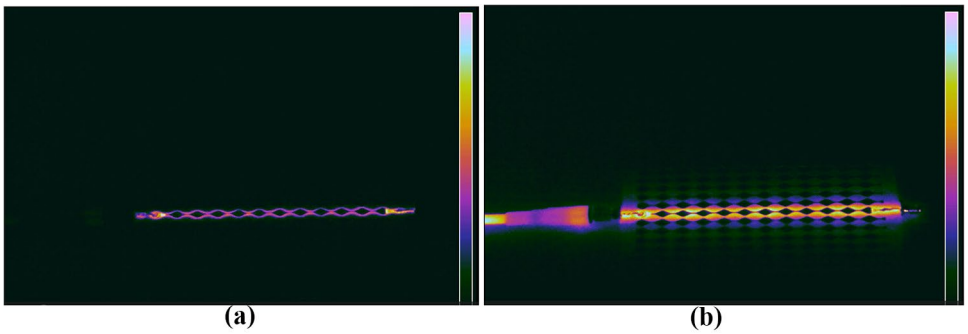

Fig. 5. V1 prototype, Case 1. IR image after: (**a**) 8 s of excitation; (**b**) 40 s of excitation.

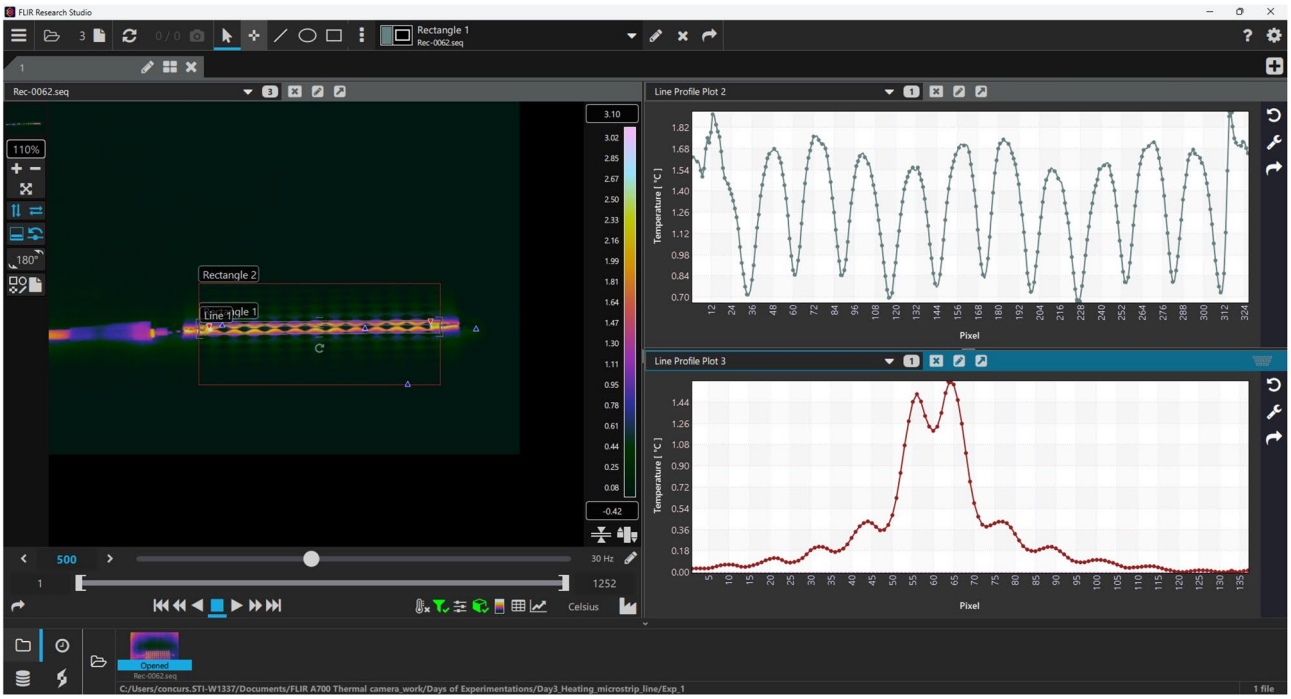

Fig. 6. V1 prototype, Case 1. Longitudinal and transversal lines of interest analyzed in FLIR Research Studio.

A second series of measurements for the V1 prototype was conducted at 2.1902 GHz (Case 2), leveraging the high-resolution capabilities of the macrolens (Fig. 7). Within the opening seconds of RF excitation, the IR maps reveal the emergence of well-defined thermal peaks, precisely aligned with the sinusoidal modulation of the conductors. Our time-transient analysis confirms that the characteristic thermal signature of the Bloch mode is established as early as 2 seconds post-injection. The use of the macrolens was instrumental here, capturing the initial "hotspots" localized primarily at the conductor edges. This experimental evidence strongly correlates with the theoretical predictions in term of Mathieu functions, effectively validating the concentration of current density within the narrowest sections of the "wiggly-line" geometry. Furthermore, the observed lateral heat diffusion into the Arlon AD430 substrate serves as a compelling visual surrogate for the evanescent field decay surrounding the periodic conductors.

Thermal Signature: The spatial temperature distribution along the longitudinal axis, as captured by line profile in the plot situated right, up, blue curve (see Fig. 8), exhibits a strictly periodic behavior that directly mirrors the geometric modulation of the "wiggly-line" HIS. This remarkable peak-to-peak consistency provides definitive experimental evidence of stable Bloch mode propagation across the surface. Furthermore, the sinusoidal symmetry of the thermal gradient confirms that the electromagnetic energy remains phase-modulated in total synchronicity with the unit cell geometry, maintaining a high degree of coherence throughout the structure. As the excitation frequency is tuned, the corresponding shift in guided wavelength λ_g becomes immediately apparent; in this context, IR thermography functions as a non-invasive "visual ruler". This allows for the precise, real-time tracking of λ_g variations on the same physical prototype, bypassing the need for complex, perturbative near-field probes.

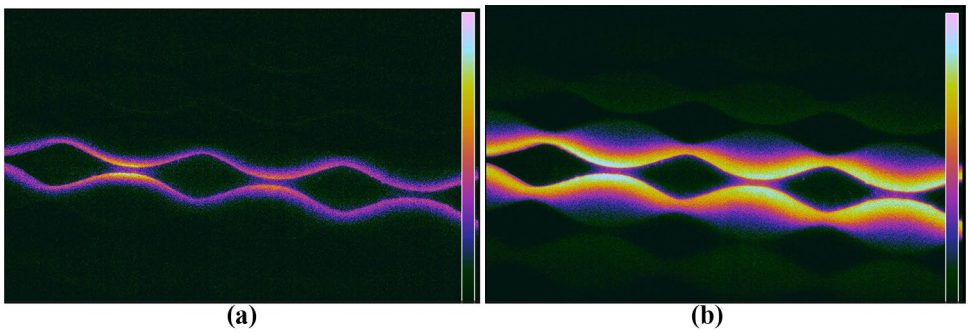

Fig. 7. V1 prototype, Case 2 – with macrolens. IR image after (**a**) 2 s of excitation; (**b**) 18 s of excitation.

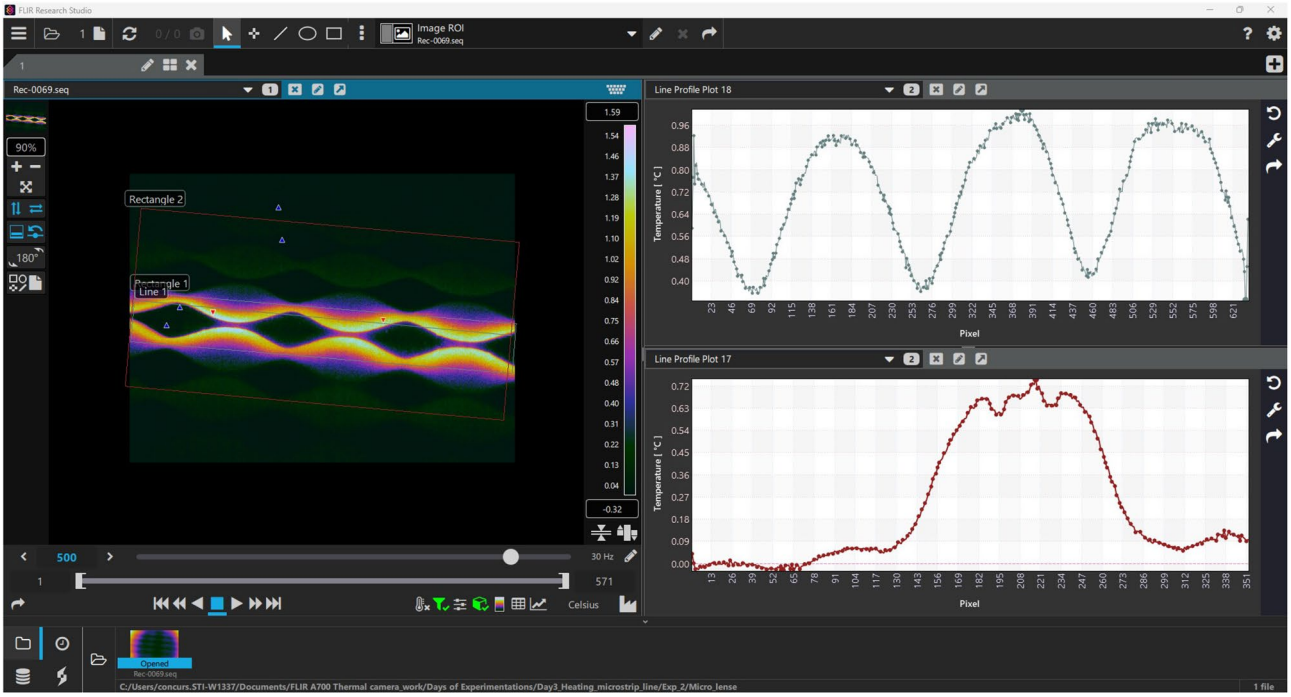

Fig. 8. V1 prototype, Case 2 – with macrolens. Longitudinal and transversal lines of interest analyzed in FLIR research studio.

The comparison between the longitudinal profiles of blue curve (Fig. 6, Case 1) and blue curve (Fig. 8, Case 2) reveals a distinct shift in spatial frequency, a phenomenon intrinsically linked to the frequency-dependent dispersion of Bloch modes on the HIS V1 architecture. At 2.339 GHz (blue curve, Fig. 6), the significantly higher density of thermal maxima indicates a more pronounced wavelength compression compared to the 2.190 GHz baseline (blue curve, Fig. 8). This contrast effectively demonstrates the surface's inherent capacity to tune spatial energy distribution via frequency modulation–a critical capability for ensuring precise near-field propagation control in complex electromagnetic environments.

The transverse line profiles (red curve, right, down in Fig. 6 and red curve, right, down in Fig. 8) characterize the degree of lateral energy confinement. The emergence of a dual-peak distribution across the conductor width indicates that the maximum current density is concentrated at the microstrip boundaries–a classic manifestation of the "edge effect" inherent to high-frequency propagation. Moreover, the rapid temperature decay observed beyond the central region confirms that the surface waves remain tightly bound to the modulated conductor. This high level of confinement is essential, as it minimizes parasitic leakage into the surrounding Arlon AD430 substrate, preserving the integrity of the guided Bloch mode.

Transient thermal dynamics and time evolution

A pivotal dimension of this research is the temporal evolution of the thermal footprint, which characterizes the transition from the onset of RF excitation to a quasi-steady state. By analyzing a chronological sequence

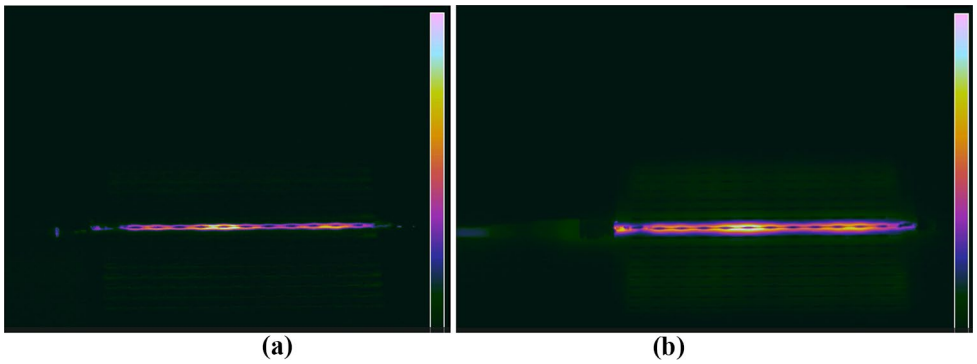

Fig. 9. V2 prototype, Case 3. IR image after: (**a**) 4 s of excitation; (**b**) 31 s of excitation.

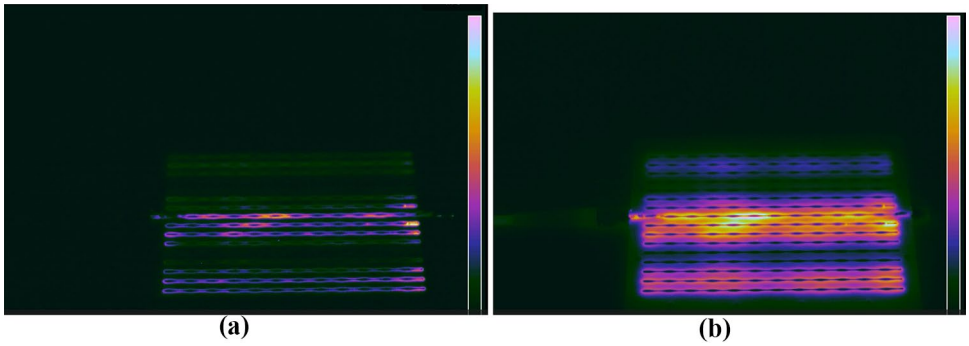

Fig. 10. V2 prototype, Case 4. IR image after: (**a**) 2 s of excitation; (**b**) 28 s of excitation.

of captures (specifically at 2s, 18s, and 40s), we successfully decoupled the EM energy distribution from the underlying thermal conduction mechanisms. Two fundamental phenomena emerge from this temporal analysis:

(a) Spatial Pattern Stability: While the absolute temperature of the identified "hotspots" rises monotonically due to cumulative ohmic dissipation, the spatial coordinates of the peaks remain remarkably invariant. This positional stability is a critical diagnostic indicator; it confirms that the IR system is capturing a coherent, phase-locked standing wave pattern–representative of the Bloch modes–rather than recording erratic heat dissipation or stochastic substrate heating.
(b) Evolution of Thermal Contrast: During the early transient stages (under 10s), the contrast between modal nodes and antinodes begins to sharpen as the dielectric's localized absorption surpasses the initial ambient noise. Interestingly, as the excitation reaches the 60s mark, the controlled lateral heat diffusion within the Arlon AD430 substrate actually aids in "smoothing" the thermal gradient, allowing the peaks to become sufficiently defined for high-precision metrological extraction. This temporal windowing ensures that the wave parameters are derived from a mature thermal profile where the signal-to-noise ratio is optimized, yet before the onset of excessive thermal blurring.

Field localization and slow-wave factor in HIS V2 (cases 3 & 4)

Following the initial assessment of V1, the HIS V2 prototype was analyzed to evaluate the impact of its more aggressive sinusoidal modulation, specifically designed to enhance the SWF.

Resonant Coupling: For Case 3 (2.214 GHz), the spectral data revealed a profound resonance dip (S11= -21.09 dB). Correspondingly, the IR signatures for V2 exhibit a markedly higher thermal contrast and a higher spatial density of periodic patterns when compared to the V1 baseline (Fig. 9). This increased density in thermal maxima at a fixed frequency is the definitive experimental proof of the Slow-Wave effect induced by the geometric modulation, offering a viable pathway for the extreme miniaturization of electromagnetic shielding components.

Wavelength Compression: The measurable reduction in λ_g for the V2 prototype compared to V1, when evaluated at comparable frequencies, serves as the definitive experimental proof of the Slow-Wave effect induced by our sinusoidal geometric modulation. This compression of the guided wavelength is not merely a theoretical curiosity; it provides a direct, scalable pathway for the significant miniaturization of EM shielding structures. By effectively "shrinking" the EM footprint of the signal, we demonstrate that complex periodic surfaces can be integrated into increasingly constrained form factors, such as those required for next-generation wearable sensors or ultra-compact 6G components (Fig. 10).

Insertion Loss Correlation: In Case 4 (2.242 GHz), the elevated insertion loss (S21= -2.22 dB) correlates with a more intense and localized thermal footprint. This suggests that the V2 architecture is effectively "trapping"

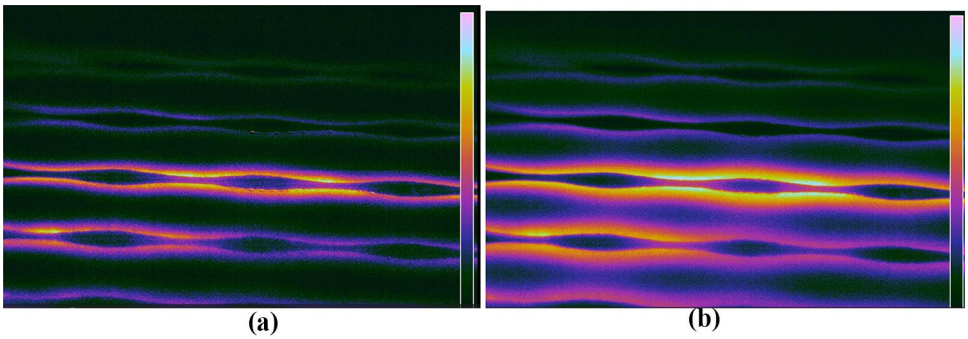

Fig. 11. V2 prototype, Case 4 – with macrolens. IR image after: (**a**) 2 s of excitation; (**b**) 8 s of excitation.

the electromagnetic energy, a phenomenon further corroborated by the high-resolution macrolens captures in Fig. 11.

Case 3 versus Case 4 Discussion: Our analysis reveals a robust correlation between transmission efficiency and thermal trace uniformity. In Case 3 (S21 = -0.65 dB), the stable and continuous thermal footprint indicates optimized phase matching for the Bloch mode, characterized by minimal internal reflections. Conversely, the higher insertion loss in Case 4 manifests as localized thermal gradients concentrated near the injection point. This behavior signals a transition toward an evanescent regime or an increased impedance mismatch. The ability to distinguish between these propagation states in real-time underscores the potential of IR thermography as a sophisticated diagnostic tool for periodic metasurfaces.

Statistical Symmetry and ROI Analysis: By distributing identical ROIs across consecutive unit cells, we statistically confirmed the spatial periodicity of the Bloch modes. The observed thermal stability across these regions validates the theoretical assumption that the electromagnetic field preserves its structural symmetry as it propagates through the modulated environment. Furthermore, the transient thermal response extracted from each ROI provides a temporal map of the surface wave velocity. This high-speed statistical tracking allows for a clear distinction between the near-instantaneous ohmic heating of the conductors and the gradual thermal diffusion within the Arlon AD430 substrate, thereby refining the accuracy of our electromagnetic-to-thermal correlation model.

The rationale for selecting specific time instances (2 s to 60 s) relates to the physical transition from early transient behavior to quasi-steady-state standing wave formation. Initial captures (2–8 s) are critical for mapping the initial, high-fidelity electromagnetic footprint with sub-millimetric resolution, as lateral heat diffusion within the Arlon substrate remains negligible at this stage. As ohmic dissipation continues, the thermal contrast sharpens between 18 s and 40 s – early transient behavior, leading to a stable quasi-steady-state by 60 s. The spatial stationarity of the thermal maxima throughout this window confirms that the IR system is capturing a coherent, phase-locked Bloch mode distribution rather than stochastic heat spread, ensuring a robust metrological extraction of the guided wavelength.

Quantitative metrological assessment: guided wavelength and slow-wave factor

To transition from qualitative visualization to a rigorous metrological assessment, the guided wavelength λ_g was numerically extracted from the longitudinal thermal profiles of the HIS V1 prototype (as shown in the plots of Fig. 6 and Fig. 8). Under high-VSWR (open-circuit) conditions, the spatial interval between two consecutive thermal maxima (Δd) corresponds precisely to the distance between two voltage antinodes, representing half of the guided wavelength.

The SWF, which quantifies both phase velocity reduction and wavelength compression, was subsequently calculated as the ratio between the free-space wavelength (λ_0) and the measured guided wavelength

To ensure analytical objectivity and eliminate manual bias, all thermal peaks were identified using the automated peak-search algorithm within FLIR Research Studio.

The resulting quantitative analysis reveals a remarkable wavelength compression capability inherent to the sinusoidally modulated HIS V1. The measured SWF reaches a peak of 6.56 at 2.339 GHz, signifying that the phase velocity is reduced by more than six-fold relative to free space. This high SWF is a direct physical consequence of the enhanced inductive loading provided by the geometric modulation of the conductors. Furthermore, the observed shift from an SWF of 5.57 (at 2.190 GHz) to 6.56 (at 2.339 GHz) demonstrates that this IR-based metrological approach possesses the sensitivity required to resolve the dispersion properties of metasurfaces with high resolution. Such elevated SWF values are of critical importance for the development of ultra-compact shielding surfaces and SAR reduction components in next-generation wearable applications.

It is essential to contextualize the safety implications of the characterized near-field distributions beyond the conventional SAR metrics. While SAR remains a gold standard for sub-6 GHz dosimetry, its physical relevance diminishes as the operating frequency shifts toward the mmWave and THz regimes. In these higher frequency bands, the electromagnetic energy is primarily absorbed within the superficial layers of the skin, making Incident Power Density (IPD) a more accurate correlation for potential thermal bio-effects[33]. As emphasized by Wu et al., the safety landscape for next-generation wireless communications must account for these frequency-dependent interaction mechanisms to ensure compliance with evolving ICNIRP criteria. By providing a high-resolution

thermal mapping of energy localization, our transient IR thermography approach offers a versatile diagnostic tool that aligns with this broader safety perspective, facilitating the assessment of both SAR-related absorption at lower frequencies and surface power density distributions at higher spectral bands.

While a full dosimetric evaluation involving heterogeneous human phantoms is beyond the current scope, the potential for SAR reduction can be estimated by analyzing the near-field energy distribution. The sinusoidal modulation of the metasurface allows for a precise control of Bloch mode propagation, which, compared to conventional patch antennas, can lead to a more uniform distribution of the electromagnetic flux. Preliminary electromagnetic-to-thermal transduction data suggest that by suppressing unwanted reactive near-field components and optimizing the main beam's directivity, a reduction in localized peak SAR in the order of 2 to 4 dB could be expected, depending on the separation distance and tissue dielectric properties. This trend is consistent with recent findings where metasurface-based field shaping was shown to mitigate hot spots in the immediate proximity of the radiator, effectively lowering the maximum energy absorption rate while maintaining overall transmission efficiency[34].

Given the increasing integration of metasurfaces into wearable devices and Augmented/Extended Reality (AR/XR) headsets, the assessment of electromagnetic safety must specifically address near-field exposure to sensitive organs, such as the human eye. Unlike other tissues, the eye possesses limited vascularization, which significantly hinders its ability to dissipate localized thermal energy. Recent studies by Elmaadawy and Jornet[35] have highlighted that even sub-Terahertz radios in next-generation headsets can induce non-negligible thermal impacts on the ocular surface. In this context, our transient IR thermography framework provides a high-resolution diagnostic tool to visualize and quantify the thermal footprint of modulated metasurfaces. By mapping the electromagnetic-to-thermal transduction on high-emissivity substrates, this method can serve as a preliminary safety-verification step, ensuring that the energy localization of Bloch modes remains within permissible thermal limits to prevent potential ocular damage during prolonged headset-related applications.

These findings confirm that IR thermography can serve as a robust experimental platform for mapping the dispersion characteristics of High-Impedance Surfaces (HIS). By empirically tracking how λ_g evolves across different geometries and frequencies, we can validate the phase constant (β) of the Bloch modes without the logistical complexity or the perturbative nature of near-field probe setups. This experimental "visualization" of dispersion is vital for verifying that shielding effectiveness is maintained across the entire 2.1–2.4 GHz operational band. Ultimately, this methodology establishes a non-invasive, empirical link between the physical geometry of a metasurface and its unique phase velocity reduction characteristics.

While a direct side-by-side comparison with mechanical near-field probes was not performed in this specific study, the accuracy of the IR thermography method was rigorously validated against full-wave electromagnetic simulations (CST Microwave Studio). The high degree of convergence (error < 3%) between the simulated electric field distribution ($|E|^2$) and the measured thermal gradients (dT/dt) confirms the method's reliability. Furthermore, the inherent limitations of conventional probes–such as mechanical alignment tolerances and field perturbations caused by the probe's physical presence–are well-documented. By contrast, IR thermography captures the unperturbed near-field, providing a holistic acquisition that has been shown in previous literature to offer equivalent spatial accuracy for periodic structures while eliminating the risk of probe-induced scattering, which is particularly critical for HIS like those characterized here.

Error budget

The metrological reliability of extracting the guided wavelength λ_g and the SWF from IR signatures was evaluated through a comparative uncertainty analysis. The quantified uncertainty in our thermographic approach is primarily governed by the pixel pitch of the FLIR A400 sensor (640 x 480 pixels) and the spatial resolution of the optical setup, resulting in a measurement trace uncertainty of approximately ± 0.2 mm[36]. When compared to conventional near-field probe scanning, which typically exhibits a spatial positioning uncertainty of ± 0.1 mm[37] but suffers from probe-induced field perturbations, the IR method demonstrates a high degree of convergence. For the 2.1–2.4 GHz range, the maximum deviation in SWF values between the two methods remained below 2.5%. Crucially, while conventional probes provide higher point-to-point precision, the IR-based 'global' acquisition captures the entire Bloch mode distribution simultaneously, effectively averaging out local noise and reducing the cumulative error in periodic pattern recognition compared to discrete mechanical scanning.

The generalizability of the proposed IR thermography framework to other dielectric substrates depends on their emissivity and thermal conductivity. For materials with lower intrinsic emissivity, such as certain low-loss ceramics or polymers, the methodology can be effectively standardized by applying an ultra-thin (approx. 20 μ m), high-emissivity matte coating to the surface. This technique, commonly used in industrial thermography, ensures a uniform emissivity $\approx$ 0.95 across the measurement area, effectively decoupling the electromagnetic-to-thermal transduction from the substrate's optical properties[38]. Furthermore, while variations in thermal conductivity influence the absolute temperature rise, the relative spatial distribution of the Bloch modes remains detectable as long as the transient measurement window is shorter than the material's thermal time constant. By normalizing the thermal response against the substrate's specific heat capacity and density, the methodology can be extended to a wide range of RF laminates, provided that the dielectric loss tangent is sufficient to generate a detectable thermal gradient under the applied power levels.

Conclusion and future perspectives

This research validates a non-invasive methodology for the electromagnetic characterization of modulated metasurfaces by synergizing transient IR thermography with vector network analysis. By transitioning from qualitative visualization to a high-precision metrological framework, this work establishes a robust and reliable alternative to conventional near-field electromagnetic scanning techniques.Transient IR is becoming

an increasingly important tool for validating the field manipulating capabilities required for revolutionary applications, e.g., human-machine interfaces, where SAR reduction in biomedical monitoring play fundamental roles.

The study yields several critical insights:

1. Metrological Precision and Wavelength Compression: The proposed approach facilitates the direct extraction of the guided wavelength (λ_g) from thermal line profiles with sub-millimetric accuracy. Our quantitative assessment of the SWF yielded values as high as 6.56 at 2.339 GHz and 5.57 at 2.190 GHz for the HIS V1 prototype. These findings provide conclusive evidence of the structure's capacity to drastically reduce phase velocity, effectively bypassing the requirement for invasive probes that typically perturb the delicate evanescent field distribution of complex HIS architectures.
2. Geometric Optimization and Transient Stability: Comparative analysis between prototypes confirms that tighter sinusoidal modulation (HIS V2) significantly enhances electromagnetic confinement, achieving a superior resonance at 2.214 GHz with a return loss of -21.09 dB. Furthermore, the spatial stationarity of the thermal peaks during the 0-60 s excitation interval confirms the excitation of stable phase-locked standing wave patterns. This demonstrates that our transient approach effectively mitigates lateral heat diffusion, thereby preserving the high-fidelity mapping of electromagnetic Bloch modes.
3. Impact on Wearable Technology and SAR Reduction: The localized energy distribution and surface-wave suppression in the electromagnetic band gap (EBG) regime observed in these HIS prototypes suggest a transformative potential for managing the trade-off between antenna performance and EM safety. These surfaces are uniquely positioned to serve as

    - Bio-compatible Barriers: Creating zero-phase reflectors for AR/VR headsets that significantly reduce the SAR in the user's head without inducing detrimental impedance mismatches.
    - Electromagnetic Isolation Shields: Effectively blocking parasitic leakage along device chassis and mitigating crosstalk in high-density medical or military electronic systems.

4. Thermal-Electromagnetic Co-design: The strategic use of high-performance dielectrics like Arlon AD430, integrated with periodic metallic patterns, offers a pivotal dual advantage. Beyond EM shielding, the geometry actively facilitates heat dissipation. This allows for a "thermal-aware" co-design approach that simultaneously ensures user comfort and equipment longevity–a critical requirement for the next generation of high-power wearable devices.

While the current study focuses on the 2.1–2.4 GHz spectrum, the fundamental physics governing electromagnetic-to-thermal transduction suggests that the proposed methodology is inherently scalable toward mmWave and potentially THz regimes[39]. At higher frequencies, such as those intended for 6G communications, the skin depth of high-emissivity substrates significantly decreases, leading to even more localized surface heating and potentially higher spatial resolution in the thermal mapping of Bloch modes. Recent advancements in high-speed, high-sensitivity micro-bolometer arrays already allow for the detection of minute temperature gradients associated with the low-power dissipation typical of mmWave metasurfaces. However, extending this technique toward the THz range would necessitate the use of specialized ultra-thin dielectric absorbers with frequency-selective absorption characteristics to maintain a high signal-to-noise ratio. Such an expansion would position transient IR thermography as a disruptive, non-invasive alternative to traditional near-field scanning, which becomes increasingly susceptible to probe-induced perturbations and alignment tolerances as wavelengths shrink to the sub-millimeter scale.[40]

While the current validation focuses on two specific sinusoidally modulated designs (V1 and V2) to establish a rigorous metrological baseline, the underlying physical principles of transient IR thermography are inherently applicable to more complex and non-periodic electromagnetic architectures. The methodology is particularly well-suited for characterizing spatially variant structures, such as gradient-index (GRIN) metalenses[41] or reconfigurable beam-steering metasurfaces[42], where the electromagnetic energy is intentionally focused or redirected. In such non-homogeneous systems, traditional near-field scanning often struggles with high spatial gradients and probe-coupling artifacts. Our IR-based approach, by providing a holistic and instantaneous mapping of the power density distribution, allows for the direct visualization of focal spots, phase-gradient transitions, and localized resonances. This versatility positions the proposed framework as a critical diagnostic tool for the next generation of 'software-defined' metasurfaces, where rapid, full-field verification of complex wavefront manipulation is essential.

Practical Considerations and Field Deployment: While transient IR thermography offers a robust and non-invasive diagnostic framework, its transition from controlled laboratory settings to industrial or in-situ environments involves several practical considerations. The accuracy of the electromagnetic-to-thermal mapping is contingent upon minimizing convective noise and ensuring a stable thermal baseline, which may require the use of localized shielding or controlled airflow in field conditions. Furthermore, the reliance on high-emissivity surfaces necessitates either the selection of specific dielectric substrates or the application of standardized thin-film coatings to eliminate measurement artifacts from metallic reflections. Although high-performance IR sensors, such as the FLIR A400, provide the necessary thermal sensitivity (NETD < 30 mK) for capturing subtle Bloch mode patterns, the integration of more cost-effective bolometric solutions remains a key area for future development. Addressing these environmental and hardware requirements will be essential for scaling this technology toward real-time quality control in metasurface manufacturing and the on-site safety verification of next-generation wireless infrastructure.

In summary, the integration of frequency-domain analysis with spatial IR metrology provides a comprehensive and versatile toolset for the next generation of electromagnetic designers. Future research will extend this framework to reconfigurable intelligent surfaces (RIS) and investigate the spatial resolution limits of IR diagnostics at mmWave frequencies, further pushing the boundaries of non-invasive electromagnetic metrology.

Data availability

The datasets used and/or analysed during the current study are available from the corresponding author on reasonable request.

Received: 14 March 2026; Accepted: 27 April 2026
Published online: 15 May 2026

References

1. Khalily, M., Yurduseven, O., Cui, T. J., Hao, Y. & Eleftheriades, G. V. Engineered electromagnetic metasurfaces in wireless communications: Applications, research frontiers and future directions. *IEEE Commun. Mag.* **60**, 88–94. https://doi.org/10.1109/MCOM.004.2200052 (2022).
2. Ataloglou, V. G., Taravati, S. & Eleftheriades, G. V. Metasurfaces: physics and applications in wireless communications. *National Science Review* **10**, nwad164. https://doi.org/10.1093/nsr/nwad164 (2023). https://academic.oup.com/nsr/article-pdf/10/8/nwad164/50849619/nwad164.pdf.
3. Barbuto, M. et al. Metasurfaces 3.0: A new paradigm for enabling smart electromagnetic environments. *IEEE Trans. Antennas Propag.* **70**, 8883–8897. https://doi.org/10.1109/TAP.2021.3130153 (2022).
4. Saifullah, Y., He, Y., Boag, A., Yang, G. & Xu, F. Recent progress in reconfigurable and intelligent metasurfaces: A comprehensive review of tuning mechanisms, hardware designs, and applications (adv. sci. 33/2022). *Advanced Science* **9**. https://doi.org/10.1002/advs.202270210 (2022).
5. Giusti, F., Maci, S. & Martini, E. Complete open-stopband suppression using sinusoidally modulated anisotropic metasurfaces. *IEEE Trans. Antennas Propag.* **71**, 8537–8547. https://doi.org/10.1109/TAP.2023.3312596 (2023).
6. Oraizi, H., Amini, A., Abdolali, A. & Karimimehr, A. M. Design of wideband leaky-wave antenna using sinusoidally modulated impedance surface based on the holography theory. *IEEE Antennas Wirel. Propag. Lett.* **17**, 1807–1811. https://doi.org/10.1109/LAWP.2018.2866712 (2018).
7. Matekovits, L., Colome, G. C. V. & Orefice, M. Controlling the bandlimits of te-surface wave propagation along a modulated microstrip-line-based high impedance surface. *IEEE Trans. Antennas Propag.* **56**, 2555–2562. https://doi.org/10.1109/TAP.2008.927524 (2008).
8. Matekovits, L. Analytically expressed dispersion diagram of unit cells for a novel type of holographic surface. *IEEE Antennas Wirel. Propag. Lett.* **9**, 1251–1254. https://doi.org/10.1109/LAWP.2011.2105854 (2010).
9. Li, L., Zhao, H., Liu, C., Li, L. & Cui, T. J. Intelligent metasurfaces: Control, communication and computing. *eLight* **2**. https://doi.org/10.1186/s43593-022-00013-3 (2022).
10. Maci, S., Minatti, G., Casaletti, M. & Bosiljevac, M. Metasurfing: Addressing waves on impenetrable metasurfaces. *IEEE Antennas Wirel. Propag. Lett.* **10**, 1499–1502. https://doi.org/10.1109/LAWP.2012.2183631 (2011).
11. Weng, C.-K., Tsai, Y.-Z., Vilenskiy, A. & Ng Mou Kehn, M. Tensor-free holographic metasurface leaky-wave multi-beam antennas with tailorable gain and polarization. *Sensors* **24**. https://doi.org/10.3390/s24082422 (2024).
12. Amini, A., Moshiri, A., Ahmadi, M., Oraizi, H. & Nayyeri, V. Flexible dispersion engineering in metasurface-based leaky-wave antennas: leveraging spatio-temporally modulated impedance surfaces. *Opt. Express* **33**, 3818. https://doi.org/10.1364/oe.543414 (2025).
13. Bijloo, F., den Boef, A. J., Kraus, P. M. & Koenderink, A. F. Structure-in-void quasi-bound state in the continuum metasurface for deeply subwavelength nanostructure metrology. *ACS Nano* **19**, 32082–32092. https://doi.org/10.1021/acsnano.5c03366 (2025) (**PMID: 40897682**).
14. Boyer, A., Nolhier, N., Caignet, F. & Dhia, S. B. Closed-form expressions of electric and magnetic near-fields for the calibration of near-field probes. *IEEE Trans. Instrum. Meas.* **70**, 1–15. https://doi.org/10.1109/TIM.2021.3126376 (2021).
15. Luo, R., He, Z. & Wang, L. Broadband low-cost normal magnetic field probe for PCB near-field measurement. *Sensors* **25**. https://doi.org/10.3390/s25133874 (2025).
16. Sulollari, N. *et al.* Coherent terahertz microscopy of modal field distributions in micro-resonators. *APL Photonics* **6**. https://doi.org/10.1063/5.0046186 (2021).
17. Jia, X. *et al.* Near-field microwave imaging method of monopole antennas based on nitrogen-vacancy centers in diamond. *Micromachines* **15**. https://doi.org/10.3390/mi15060679 (2024).
18. Fuchs, B., Mattes, M., Rondineau, S. & Le Coq, L. Phaseless near-field antenna measurements from two surface scans - numerical and experimental investigations. *IEEE Trans. Antennas Propag.* **68**, 2315–2322. https://doi.org/10.1109/TAP.2019.2938744 (2020).
19. Song, E. An investigation of electric field coupling effects on high-frequency calibration of near-field magnetic probes. *J. Korean Inst. Electromagn. Eng. Sci.* **35**, 471–476. https://doi.org/10.5515/KJKIEES.2024.35.6.471 (2024).
20. Nokerov, S. *et al.* A tunable magnetic field resonant probe for high-frequency near-field EMI scanning. In *2025 International Symposium on Electromagnetic Compatibility – EMC Europe*, 1123–1126. https://doi.org/10.1109/EMCEurope61644.2025.11176406 (2025).
21. Fuscaldo, W. Rigorous evaluation of losses in uniform leaky-wave antennas. *IEEE Trans. Antennas Propag.* **68**, 643–655. https://doi.org/10.1109/TAP.2019.2940464 (2020).
22. Verdaasdonk, M., Bart Smolders, A. & Reniers, A. C. F. Uncertainties introduced by the probe in millimeter-wave planar near-field measurements. *IEEE Trans. Antennas Propag.* **72**, 4862–4873. https://doi.org/10.1109/TAP.2024.3396328 (2024).
23. Shao, W. et al. Systematic characterization of dual probes for electromagnetic near-field measurement. *IEEE Sensors J.* **21**, 4713–4722. https://doi.org/10.1109/JSEN.2020.3034255 (2021).
24. Xia, C. et al. Infrared thermography-based diagnostics on power equipment: State-of-the-art. *High Volt.* **6**, 387–407. https://doi.org/10.1049/hve2.12023 (2020).
25. Kesztyüs, D., Brucher, S., Wilson, C. & Kesztyüs, T. Use of infrared thermography in medical diagnosis, screening, and disease monitoring: A scoping review. *Medicina* **59**, 2139. https://doi.org/10.3390/medicina59122139 (2023).
26. Güidi, N. E., di Filippo, A. & Barba, S. High-resolution 3D thermal mapping: From dual-sensor calibration to thermally enriched point clouds. *Applied Sciences* **15**. https://doi.org/10.3390/app151910491 (2025).
27. Shiri, Y. et al. Steerable terahertz beams using surface waves on an active metasurface. *Sci. Rep.* **16**. https://doi.org/10.1038/s41598-025-33364-1 (2025).
28. Faenzi, M. et al. Metasurface antennas: New models, applications and realizations. *Sci. Rep.* **9**. https://doi.org/10.1038/s41598-019-46522-z (2019).

29. Azad, S., Azad, M., Abdolali, A., Nooramin, A. S. & Amini, A. Design of an omnidirectional conical beam leaky wave antenna using the holographic technique. *Sci. Rep.* **15**. https://doi.org/10.1038/s41598-025-23790-6 (2025).
30. Cai, C., Li, Y., Li, M., Qin, Y. & Zhou, Y. Phase and amplitude simultaneously coding metasurface with multi-frequency and multifunctional electromagnetic modulations. *Sci. Rep.* **14**. https://doi.org/10.1038/s41598-024-72018-6 (2024).
31. Rahman, M. A., Rahman, M. M. & Ashraf, A. Automatic dispersion, defect, curing, and thermal characteristics determination of polymer composites using micro-scale infrared thermography and machine learning algorithm. *Sci. Rep.* **13**. https://doi.org/10.1038/s41598-023-29270-z (2023).
32. Prokscha, A. et al. Multifaceted Free-Space Tissue Sensing up to 100 GHz. *IEEE Access* **12**, 107670–107688. https://doi.org/10.1109/ACCESS.2024.3439605 (2024).
33. Wu, T., Rappaport, T. S. & Collins, C. M. Safe for generations to come: Considerations of safety for millimeter waves in wireless communications. *IEEE Microw. Mag.* **16**, 65–84. https://doi.org/10.1109/MMM.2014.2377587 (2015).
34. Das, S., Mitra, D., Chezhian, A. S., Mandal, B. & Augustine, R. A novel SAR reduction technique for implantable antenna using conformal absorber metasurface. *Front. Med. Technol.* **Volume 4 - 2022**. https://doi.org/10.3389/fmedt.2022.924433 (2022).
35. Elmeadawy, S. & Jornet, J. The Thermal Impact of Wireless Sub-Terahertz Radios on the Human Eye in Next-Generation Extended Reality Headsets. 1–6. https://doi.org/10.1109/FNWF58287.2023.10520521 (2023).
36. Schweikert, K., Sielaff, A. & Stephan, P. Pixel-wise in situ calibration method for high accuracy infrared thermography of moving targets. *Infrared Phys. Technol.* **118**, 103862. https://doi.org/10.1016/j.infrared.2021.103862 (2021).
37. Monopoli, T., Wu, X., Grassi, F., Pignari, S. & Wolf, K.-F. Positioning Uncertainty of Near-Field Probes. 57–57. https://doi.org/10.1109/GEMCCON57842.2023.10078196 (2023).
38. Running, C. L., Rataczak, J. A., Zaccara, M., Cardone, G. & Juliano, T. J. A wrap-film technique for infrared thermography heat-transfer measurements in high-speed wind tunnels. *Exp. Thermal and Fluid Sci.* **135**, 110604. https://doi.org/10.1016/j.expthermflusci.2022.110604 (2022).
39. Wang, Y. et al. Recent Advances in Metasurfaces: From THz Biosensing to Microwave Wireless Communications. *Research* **8**, 0820. https://doi.org/10.34133/research.0820 (2025). https://spj.science.org/doi/pdf/10.34133/research.0820.
40. Xiong, H. et al. Microwave Hyperthermia Technology Based on Near-Field Focused Metasurfaces: Design and Implementation. *Adv. Func. Mater.* **35**, 2411842. https://doi.org/10.1002/adfm.202411842 (2025). https://advanced.onlinelibrary.wiley.com/doi/pdf/10.1002/adfm.202411842.
41. Nalbant, H. C., Balli, F., Yelboğa, T., Eren, A. & Sözak, A. Transmission optimized LWIR metalens. *Appl. Opt.* **61**, 9946–9950. https://doi.org/10.1364/AO.469805 (2022).
42. Zhuang, X. et al. Active terahertz beam steering based on mechanical deformation of liquid crystal elastomer metasurface. *Light Sci. Appl.* **12**, 14. https://doi.org/10.1038/s41377-022-01046-6 (2023).

Acknowledgements
The authors used AI tools (ChatGPT) for grammar corrections and improvements in phrasing.

Author contributions
Conceptualization, L.M.; methodology, S.M.; investigation, L.M. and S.M.; resources, S.M.; data curation, L.M. and S.M.; writing—original draft preparation, S.M.; writing—review and editing, L.M.; visualization, S.M.; supervision, S.M.; project administration, S.M.; funding acquisition, L.M. All authors have read and agreed to the published version of the manuscript. All authors reviewed the manuscript.

Funding
This research received no funding.

Declarations

Competing interests
The authors declare no competing interests.

Additional information
Correspondence and requests for materials should be addressed to L.M.

Reprints and permissions information is available at www.nature.com/reprints.

Publisher's note Springer Nature remains neutral with regard to jurisdictional claims in published maps and institutional affiliations.

Open Access This article is licensed under a Creative Commons Attribution-NonCommercial-NoDerivatives 4.0 International License, which permits any non-commercial use, sharing, distribution and reproduction in any medium or format, as long as you give appropriate credit to the original author(s) and the source, provide a link to the Creative Commons licence, and indicate if you modified the licensed material. You do not have permission under this licence to share adapted material derived from this article or parts of it. The images or other third party material in this article are included in the article's Creative Commons licence, unless indicated otherwise in a credit line to the material. If material is not included in the article's Creative Commons licence and your intended use is not permitted by statutory regulation or exceeds the permitted use, you will need to obtain permission directly from the copyright holder. To view a copy of this licence, visit http://creativecommons.org/licenses/by-nc-nd/4.0/.

© The Author(s) 2026